Research article

Developing zinc oxide and peanut shell-derived carbon star-shaped composite materials for effective photo-antibacterial treatment

Fasih Bintang Ilhami [a,**], Fitriana [b], Tjandrawati Mozef [c], Muh Nur Khoiru Wihadi [d], Munasir [b], Mufidatul Khasanah [a], Nugrahani Primary Putri [b], Diah Hari Kusumawati [b], Chen-Yu Kao [e], Dong-Hau Kuo [f], Noto Susanto Gultom [f,g,*]

[a] Department of Natural Science, Faculty of Mathematics and Natural Science, Universitas Negeri Surabaya, Surabaya, 60231, Indonesia
[b] Department of Physics, Faculty of Mathematics and Natural Science, Universitas Negeri Surabaya, Surabaya, 60231, Indonesia
[c] Research Center for Pharmaceutical Ingredients and Traditional Medicine, National Research and Inovation Agency, Tangerang Selatan, 15314, Indonesia
[d] Research Center for Chemistry, National Research and Innovation Agency (BRIN), Republik Indonesia, Kawasan Sains dan Teknologi (KST) B. J. Habibie, Tangerang Selatan, 15311, Indonesia
[e] Graduate Institute of Biomedical Engineering, National Taiwan University of Science and Technology, Taipei, 10607, Taiwan
[f] Department of Materials Science and Engineering, National Taiwan University of Science and Technology, No.43, Sec. 4, Keelung Road, Taipei, 10607, Taiwan
[g] Department of Physics, Universitas Padjadjaran, Bandung, 45363, Indonesia

ARTICLE INFO

ABSTRACT

The development of new carbon-based materials using natural biowaste for biomedical applications has remained a significant challenge in the past decades. In this study, we successfully synthesized and characterized composite materials made from peanut shell-derived carbon (PNS–C) decorated on ZnO that formed star-shaped particles via a simple hydrothermal technique. The as-prepared composites possess several advantages, including unique optical properties and high photostability. We evaluate the antibacterial performance against *Escherichia coli*, a gram-negative bacterium and *Staphylococcus aureus*, a gram-positive bacterium, under irradiated and non-irradiated conditions. Interestingly, the photo-antibacterial activities of ZnO/PNS-C composites showed great inhibition of bacterial growth as compared to pure ZnO. Moreover, significant disruptions in cellular activities occur when the composites make direct contact with the bacterial cell wall. The electrons and holes produced by excitation in composites provide a pronounced deactivating effect on bacterial activity. In addition, ZnO/PNS-C composites are highly biocompatible with normal cells. Thus, these newly developed composites made from a natural biowaste system with an affordable price, abundance, and non-toxicity could provide a potentially environmentally friendly and fruitful route for antibacterial therapy in future applications.

* Corresponding author. Department of Materials Science and Engineering, National Taiwan University of Science and Technology, No.43, Sec. 4, Keelung Road, Taipei, 10607, Taiwan.
** Corresponding author. Department of Natural Science, Faculty of Mathematics and Natural Science, Universitas Negeri Surabaya, Surabaya, 60231, Indonesia

E-mail addresses: fasihilhami@unesa.ac.id (F.B. Ilhami), noto.susanto.gultom@unpad.ac.id (N.S. Gultom).

1. Introduction

Microbial infections have posed a significant challenge to public health throughout history, prompting ongoing endeavors to address these infections, such as the development of novel drugs and antibiotics [1–5]. Pathogens, however, have been defined as having the ability to resist single or multiple antibiotics due to the widespread distribution and misappropriation of antibiotics over the past few decades [6,7]. Several alternatives to displaced antibiotics have been developed, including antibacterial nanosilver materials [8], photocatalytic disinfection [9], antibacterial photocatalytic therapy (APCT) [10] and photodynamic therapy [11]. Among these alternatives, photodynamic therapy has gained a lot of interest due to one of the most effective sterilization technologies, a process that entails the production of reactive oxygen species (ROS) by activating a photosensitizer by light and the presence of oxygen [12,13]. Several types of photosensitizers have been investigated in photodynamic therapy, such as silver nanoparticles [14], TiO_2 [15], copper [16], g-C_3N_4 [17], porphyrin derivatives [18], phthalocyanines [19], ZnO [20,21] and carbon-based materials [22]. However, these photosensitizers have shortcomings that limit their development as antimicrobials: (1) the inability to prevent bacterial growth; (2) a narrow absorption range; (3) poor stability, which is a potential leak into the environment. Therefore, the development of antimicrobial particles with characteristics of low-cost, abundance, low toxicity, and stability is required for extensive use.

Recently, Carbon-Based Materials (CBMs), such as carbon nanotubes (CNTs), graphene, mesoporous carbon nanoparticles, and carbon quantum dots have shown significant promise as a novel class of photoactivated antimicrobial agents. Specifically, CBMs possess several advantageous properties, including high surface areas [23], excellent optical properties [24], distinctive electrical and thermal conductivity properties [25], and excellent antibacterial properties [26]. Moreover, the surface area of CBMs consists of many carboxylic acids, which gives them readily solubility in an aqueous solution and is suitable for functionalization with other two-dimensional (2D) materials, polymeric nanoparticles, or porphyrin derivatives containing amino groups to facilitate efficient surface passivation [27]. Importantly, CBMs are easily activated by visible light linked to photoinduced redox processes, which significantly broadens their application to kill cancer cells and antimicrobial agents [28]. Generally, when CBMs are photoexcited to initiate the anticipated effective charge transfer and separation, the resulting electron-hole pairs, along with the luminescent excited states generated from their radiative recombination, may be linked to the potent photodynamic effects and the generation of ROS, leading to the observed eradication of both cancer cells and bacterial cells [29]. The price of referred material precursors is typically a fundamental consideration in synthesizing CBMs. Thus, it is necessary to greenly synthesize the antibacterial materials derived from biowaste like peanut shells through a simple hydrothermal technique due to the only a few papers that have reported the antibacterial properties of peanut-derived CBMs.

Zinc oxide (ZnO), an n-type semiconductor from the II–VI group, is characterized by its large band gap value of about 3.3 eV. It is a compelling material because it works well as a photocatalyst, is cheap, and is simple to synthesize in both bulk and nanostructured forms [30,31]. Several researchers have investigated ZnO as an antimicrobial agent on a nano- and micro-scale due to the fact that the surface of ZnO can interact with the surface of bacteria and/or with a core of bacteria, subsequently penetrating into the core of cells and subsequently inhibiting bacterial growth [32]. Another unique property of ZnO is that it can serve as a promising photosensitizing agent owing to its distinctive photocatalytic properties when exposed to light radiation [33,34]. Importantly, ZnO has the capacity to produce ROS on its surface, potentially leading to cell death when the ROS levels surpass those counteracted by its antioxidants [35]. It is regarded that the combination of the carbon-based material and ZnO can result in distinctive physical, chemical properties and photo-antibacterial activity.

Very recently, some green synthetic approaches using cheap, renewable, and eco-friendly biomass resources as carbon sources using a single step have induced great interest. The peanut shell stands out as one of the most abundant agricultural wastes in key peanut-producing countries such as Vietnam, China, and Indonesia [36]. Peanut shells are often undervalued, and a significant portion is casually discarded, disregarding their potential utility, which contradicts the principles of sustainability and waste recycling. Recent studies mentioned that peanut shells can be effectively employed in various applications, including dye adsorption, salt-induced soil improvement, and the production of activated carbon as living cell imaging [37–39]. Hence, there is a strong inclination to investigate alternative biowaste-based precursors for biomedical applications through green synthesis methods.

Herein, we develop a star-shaped ZnO/PNS-C composite made of peanut shell-derived carbon (PNS–C) decorated with ZnO for photo-antibacterial therapy. The natural bio-waste of peanut shell was carbonized to form a carbon layer material, subsequently composited with a zinc acetate precursor through a hydrothermal technique with a slightly adapted green chemistry method in a one pot process from Boukherroub and co-workers [40]. These composites possess several advantages, such as star-shaped particles and high photostability. More importantly, star-shaped ZnO/PNS-C composite exhibited great inhibition of bacterial growth compared to pure ZnO as an antibacterial agent after light irradiation. Interestingly, the ZnO/PNS-C composite is highly biocompatible with normal cells. Therefore, this newly developed composite from a natural biowaste system potentially serves as an environmentally friendly antibacterial therapy for a wide range of biomedical applications.

2. Experimental section

2.1. Materials

Peanut shells used in this study were obtained from local farming near Surabaya, Indonesia. Zinc acetate dihydrate [Zn(CH$_3$COO)$_2$.2H$_2$O] and sodium hydroxide (NaOH) were purchased from Merck (Germany) with the highest purity available. The ultrapure water was purified using Milli-Q plus 185 equipment and consistently employed in all experimental procedures conducted in

this study.

2.2. Synthesis

2.2.1. Synthesis of peanut shell-derived carbon

The pyrolysis method was used to produce peanut shell-derived carbon (PNS–C). Briefly, the peanut shell was placed inside a ceramic crucible and heated at 250 °C for 2 h with a heating rate of 10 °C min^{-1}. Once the temperature reached room temperature, the dark black products were then subjected to a mechanical grinding process to produce a fine powder. Next, 0.1 g of the resulting sample was dissolved in 50 mL of distilled water by ultrasonication for about 30 min. Finally, peanut shell-derived carbon was collected by filtering out larger particles using a filtration membrane with a pore size of 0.22 μm and stored at 4 °C for further characterization and usage.

2.2.2. Preparation of ZnO/PNS-C composites

The hydrothermal method was used to synthesize ZnO/PNS-C composite. 0.1 g of Zn(CH$_3$COO)$_2$ was dissolved in purified 10 mL water and direct blending with 40 mL of PNS-C solution under steady stirring. Subsequently, the pH of the mixture solution was adjusted to 10 by adding NaOH solution and followed by agitating process for 15 min at ambient temperature. Then, the mixture solution was transferred into a 50 mL Teflon-lined autoclave and heated at 150 °C for 3 h. The final product was obtained by the centrifugation process, and then it was rinsed many times with deionized water in order to eliminate any impurities. The preparation of the ZnO/PNS-C composite is schematically illustrated in Scheme 1. The pristine ZnO was obtained by a similar method without the incorporation of the PNS-C solution.

2.3. Characterization

2.3.1. UV–vis spectrophotometry

The optical absorption of samples was recorded using a UV-1900 (Shimadzu, Japan) spectrophotometer at wavelength of 200–800 nm.

2.3.2. Photoluminescence spectrophotometry

The fluorescence intensity of pristine PNS-C and ZnO/PNS-C composites were determined using a photoluminescence spectrometer with an excitation wavelength of 310 nm and a scanning range of 290–800 nm.

2.3.3. Fourier transform infrared spectroscopy (FTIR)

Fourier transform infrared (FTIR) measurements were collected from KBr pellets using a Shimadzu IRTracer-100 spectrophotometer to analyze the chemical composition of pristine PNS-C, ZnO, and ZnO/PNS-C composites. Then, the spectra of the samples were scanned at a range from 600 to 4000 cm^{-1}
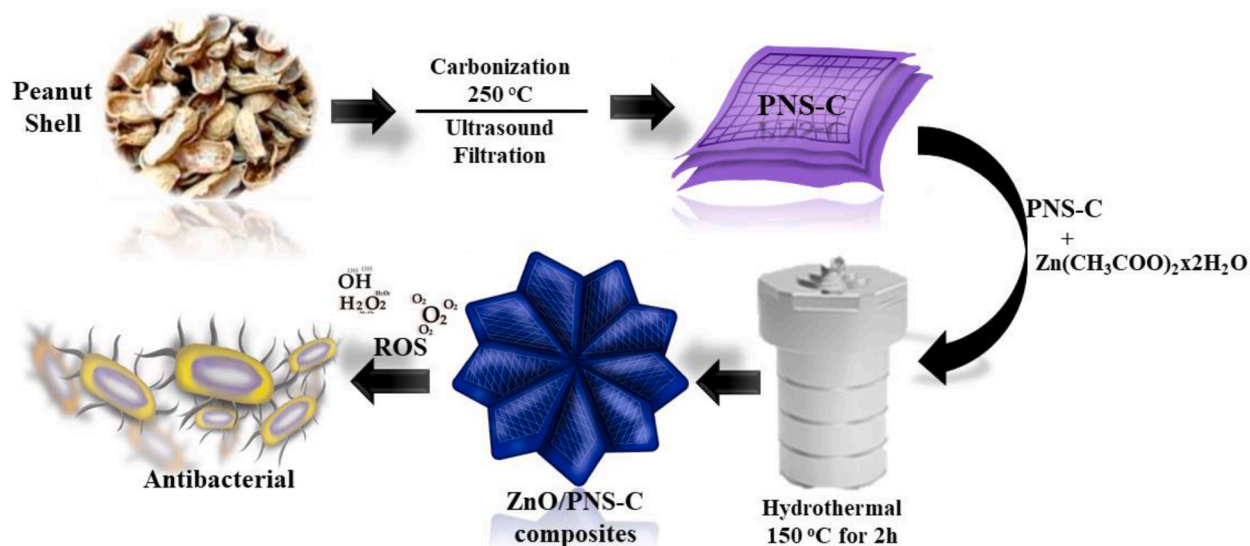
Scheme 1. Graphical illustration for the synthesis of star-shaped composites through peanut shell-derived carbon decorated on ZnO (ZnO/PNS-C) and absorbed specific light to generate reactive oxygen species for antibacterial therapy.

2.3.4. Powder X-ray diffraction (PXRD)

The X-ray diffraction (XRD) patterns were obtained using a Miniflex-600 X-ray diffractometer (Rigaku, Japan) in the range of 10–80° equipped with Cu K_α radiation ($\lambda = 1.5419$ Å) at 30 kV and 10 mA.

2.3.5. Scanning electron microscopy

A field-emission scanning electron microscopy FE-SEM (JSM6500, JEOL, Tokyo, Japan) equipped with an energy-dispersive X-ray spectroscopy (EDS) were conducted to observe the morphology and elemental composition of pristine PNS-C and ZnO/PNS-C composites.

2.3.6. Electron Paramagnetic Resonance

The hydroxyl ROS was detected using Electron Paramagnetic Resonance (EPR-Plus, Bruker) at room temperature. 2 mg of the sample was dispersed in 1 mL DI water by ultrasonication for about 30 min. Then, 0.1 mL DMPO reagent (0.1 M) was added to above solution before EPR measurement.

2.4. Bacterial culture

A solitary colony of *Escherichia coli* (*E. coli*; as a gram-negative bacterium) and *Staphylococcus aureus* (*S. aureus*; as a gram-positive bacterium) was utilized for this study. These microorganisms were cultured in lysogeny broth (LB) at 37 °C.

2.5. Minimal inhibitory concentration antibacterial test

The minimal inhibitory concentration (MIC; μg/mL) is characterized as the lowest concentration of the novel compounds that entirely halted bacterial growth, achieved through the standard method of serial dilution by a factor of two in 96-well micro-test plates. The bacteria growth was monitored via spectrophotometry.
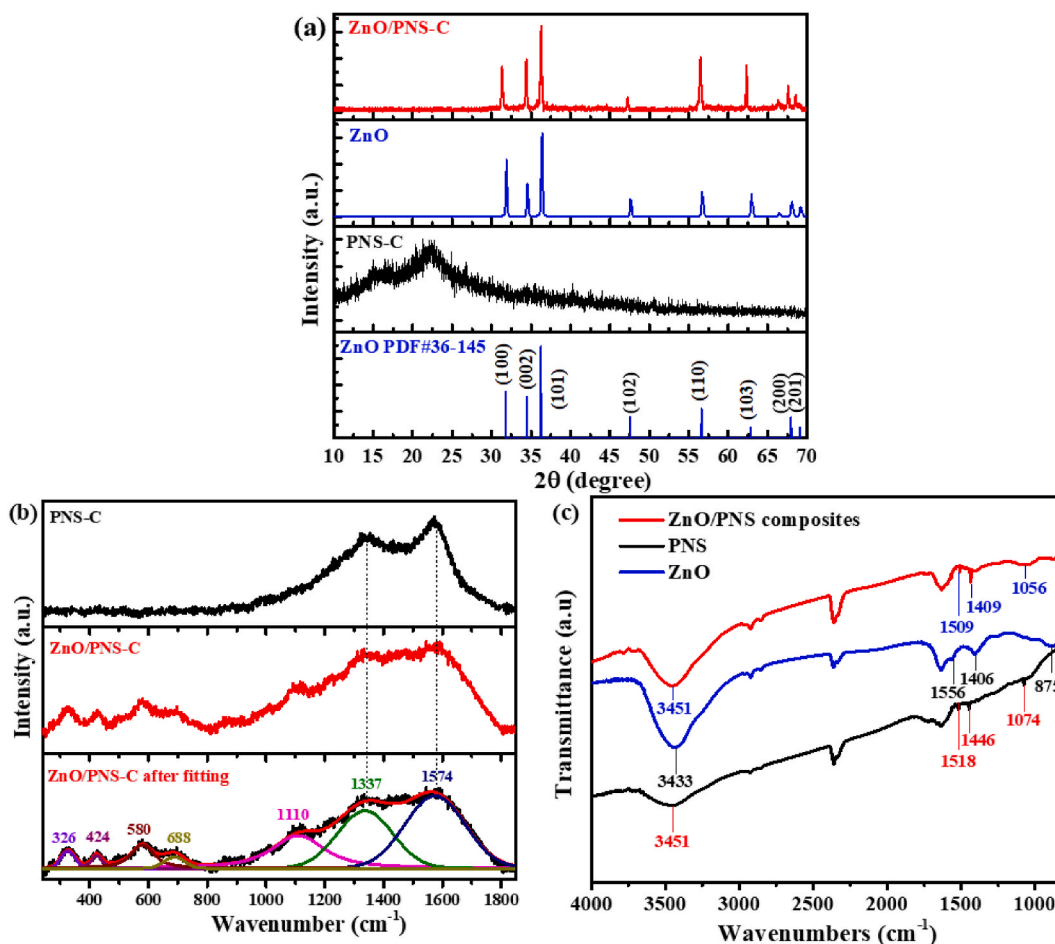

Fig. 1. **(a)** XRD patterns, **(b)** Raman spectra, and **(c)** FTIR spectra of pristine PNS-C, ZnO, and ZnO/PNS-C composites.

2.6. Antibacterial assay

The spread plate method was employed to assess the antibacterial ability. *E. coli* and *S. aureus* were treated with pristine PNS-C, ZnO, and ZnO/PNS-C composite. Then, the bacterial sample was exposed to irradiation and without irradiation for 10 min using a light source emitting with a wavelength of 635 nm and an intensity of 50 mW/cm^2 before being added to the cell suspension, while untreated bacteria were kept as a control group. Next, all groups were incubated at 37 °C for 2 h. The bacterial solution was diluted with PBS. 10 μL of the bacterial solution was plated on LB agar and subjected to culturing at 37 °C. After 24 h, the bacterial colonies on the plate were analyzed.

2.7. Cellular toxicity studies

Raw cells 264.7 were cultured in 96-well plates first for 24 h in an incubator (37 °C, 5 % CO$_2$) and continued for another 24 h after the culture medium was replaced by 100 μL of fresh medium containing ZnO/PNS-C with different concentrations (0, 50, 100, 150, 200, and 250 μg/mL). Then, 10 μL of the MTT were added to each well for further incubation for 4 h. Subsequently, unreacted dye was removed and 100 μL DMSO was added to dissolve the remaining blue formazan. Finally, the absorbance values were determined using an automatic microplate reader at wavelength of 570 nm.

3. Results and discussion

3.1. Structural properties

The crystal structure of our sample was initially analyzed using the X-ray diffraction (XRD) technique, as depicted in Fig. 1a. The XRD pattern of the PNS-C exhibited a broad peak located at approximately 23.26°, which is associated with the presence of highly disordered carbon atoms, indicating the amorphous structure. This information confirms the existence of carbon materials derived from our peanut shell. The XRD pattern of the pristine ZnO clearly shows several high intensity peaks at 2θ = 31.34°, 34.40°, 36.23°, 47.25°, 56.42°, 62.29°, 66.32°, 67.55°, and 68.4°, similar to our previous work [41]. Based on the data standard file of PDF #36–1451, those peaks suggest the successful formation of the ZnO with a hexagonal/wurtzite crystal structure, attributing to the (100), (002), (101), (102), (110), (103), (200), and (201) planes. The XRD pattern of the ZnO/PNS-C composite was not significantly different as compared to that of pristine ZnO. This XRD pattern was unable to prove the presence of the carbon peak in the composite sample. Therefore, we further conducted Raman spectroscopy analysis, which is powerful to confirm the presence of carbon-based material [42]. As depicted in Fig. 1b, the Raman spectra of the PNS-C clearly show two distinct peaks at wavenumbers of 1337 and 1574 cm^{-1}, corresponding to the D and G bands of the carbon, respectively. The Raman spectra of ZnO/PNS-C show a similar pattern to that of pristine PNS-C, with several extra peaks at low wavenumbers. To precisely determine those Raman peaks, we performed the deconvolution technique. After fitting process, several peaks can be found at wavenumber of 326, 424, 580, 685 and 1110 cm^{-1} correspond to the characteristic of ZnO with 2E2, E2, A1-LO, 2(E2H-E2L), and A1(TO) + E1(TO) + E2L modes, respectively [43,44]. It is then clear that Raman analysis provides strong evidence of the success of ZnO/PNS-C composite formation. FTIR analysis with a transmission mode was conducted to further evaluate the presence of PNS-C within the ZnO/PNS-C composite heterostructures and explore the interaction between ZnO and PNS-C. As shown in Fig. 1c–a peak at 875 cm^{-1} indicates Zn–O vibrations and a broad band at 3433 cm^{-1} is attributed to stretching –OH groups from surface-adsorbed water molecules [45,46]. The bands at 1400 and 1574 cm^{-1} are linked to highly attributed residual acetate groups within the material. Moreover, the FTIR spectrum of the PNS-C showed a prominent and wide peak corresponding to the stretching vibration mode of O–H bonds observed at 3451 cm^{-1}. The band observed at 1518 cm^{-1} attributed to the stretching of C=C bonds in polycyclic aromatic hydrocarbons, whereas the peaks at 1074 and 1446 cm^{-1} correspond to vibrations of C–O bonds in oxygen-containing groups which provides excellent water solubility [47]. On the other hand, the FTIR spectrum of the ZnO/PNS-C composite displayed peaks at 3451, 1509, 1409, and 1056 cm^{-1}. These results presented a slight blue shift observed in the peaks that can be attributed to the interaction between ZnO and PNS-C [48].

To further evaluate the crystal properties of our samples, we derived some properties such as crystallite size, dislocation density, d-spacing value, macro-strain, and lattice parameters. The equations for computing those properties are listed in Eqs. (1)–(6) [49]. It should be noted that only the crystalline sample can be analyzed. Pure PNS-C is not listed in Table 1 due to its amorphous structure. As summarized in Table 1, the crystal properties of the pristine ZnO and ZnO/PNS-C did not significantly different, indicating that the incorporation of the PNS-C did not disturb the crystal growth or the crystal structure of the ZnO.

Table 1
Summary of crystal properties of pristine ZnO and ZnO/PNS-C composite.

Samples	FWHM/β (rad)	Crystallite size (nm)	Dislocation density x 10^{-4} (nm^{-2})	d-spacing at (101) plane	Macro strain values <e>	Lattice parameters (Å)	
						a	c
ZnO	0.205	40.66	6.05	2.467	3.57×10^{-3}	3.237	5.187
ZnO/PNS-C	0.217	38.52	6.74	2.473	0.91×10^{-3}	3.297	5.209

$$D = \frac{0.9\lambda}{\beta \cos \theta} \qquad \text{(eq. 1)}$$

Where, D is the crystallite size (nm), λ is the wavelength (nm), β is the full half maximum, FWHM full-width half maximum (rad), and θ is Bragg angle (°).

$$\delta = \frac{1}{D^2} \qquad \text{(eq. 2)}$$

$$\langle e \rangle = \frac{d - d_o}{d_o} \qquad \text{(eq. 3)}$$

Where, d_o is the interplanar spacing of pristine ZnO and d is the calculated interplanar spacing at (101) plane using Bragg law.

The lattice parameters a and c can be calculated using the equation

$$a = \frac{\lambda}{\sqrt{3} \sin \theta_{(100)}} \qquad \text{(eq. 4)}$$

$$c = \frac{\lambda}{\sin \theta_{(002)}} \qquad \text{(eq. 5)}$$

To gain insight into the surface morphology and microstructure of our samples, a scanning electron microscopy (SEM) equipped with energy dispersive spectroscopy was conducted at a working voltage of 15 kV. Fig. 2a and **d** depict the morphology of PNS-C,
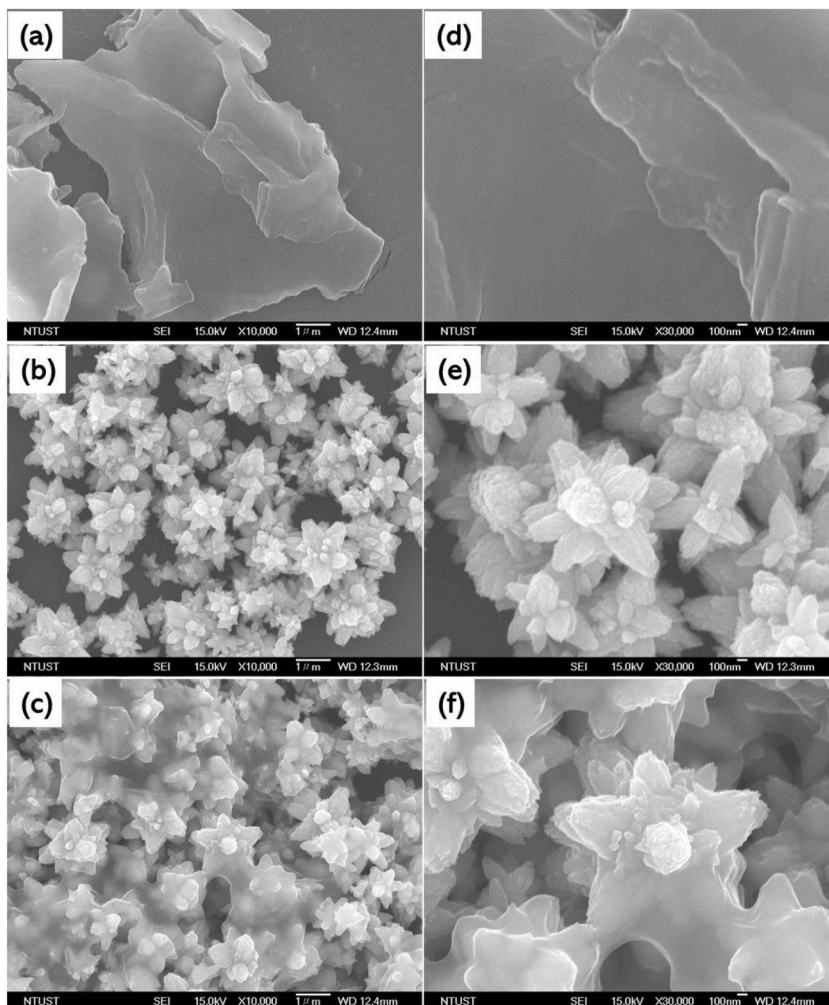

Fig. 2. Scanning electron microscope images of low and high magnifications PNS-C **(a,d)**, ZnO **(b,d)**, and ZnO/PNS-C composite **(c,f)**.

which is uniformly disseminated with layer-by-layer morphology. The pristine ZnO prepared by the hydrothermal method shows a unique morphology of micro star-shape with a uniform and regular size, as shown in Fig. 2b and e. Interestingly, ZnO/PNS-C composites displayed like star-shaped stacked layer-by-layer morphology due to interaction between ZnO and the PNS-C layer, subsequently, ZnO is encapsulated by the 2-D layer of the PNS-C layer (Fig. 2c and f).

The atomic percentages of each element in our samples were determined using the EDS analysis, as tabulated in Table 2. The pure PNS-C shows the presence of carbon at more than 70 % and oxygen at about 30 %. The pristine ZnO consists of Zn and O with atomic percentages of 38 % and 62 %, respectively. However, the composite sample shows the presence of C, Zn, and O with percentages of 41.8, 14.6, and 43.6 %, respectively, indicating the success of the ZnO/PNS-C composite formation. To further verify the element distribution, we conducted an EDS mapping analysis using the ZnO/PNS-C composite sample. As depicted in Fig. 3, each element of the ZnO/PNS-C composite, including Zn, O, and C is regularly and uniformly distributed throughout the entire area of mapping acquisition.

3.2. Optical properties

The optical profiles of pristine PNS-C, ZnO and ZnO/PNS-C composite were studied using a UV–Vis spectrophotometer. The results of the absorption properties are depicted in Fig. 4a. The characteristic absorption of ZnO is located at the UV region with peak absorption at a wavelength of 335 nm. The absorbance spectrum of PNS-C exhibited a broader range, with significant absorption extending into the near-infrared region. Interestingly, ZnO/PNS-C composite showed broad optical absorbance and were slightly red-shifted (345 nm) due to the highly planar π-conjugated structure, and improved the delocalization of π-electrons within the 2D skeleton [50]. More importantly, the absorption of the composite sample is much higher than those of pristine PNS-C and ZnO, suggesting its capability to absorb much more light intensity as compared to those PNS-C and ZnO. The charge carrier dynamics were further investigated by measuring the emission spectra using photoluminescence (PL) spectroscopy, as depicted in Fig. 4b. The ZnO/PNS-C composite exhibited clear emission peaks at 435 nm, which were slightly to blue-shifted and had a high intensity of about 1200 a. u. This is in contrast to the intensity of PNS-C, which was only 650 a.u, It is widely acknowledged that the quantity of photo-generated charges is directly proportional to the light absorption value [51]. Fig. 4a reveals that the light adsorption value of the composite material is ten times greater than that of pure ZnO. This indicates that the number of photo-generated charges is also ten times greater, thereby increasing the possibility of electron-hole recombination by the same factor of ten. Consequently, despite the fact that the PL emission indicates that the composite material possesses a twofold increase in intensity compared to pure ZnO, this observation is reasonable, and it is still possible to conclude that the composite's formation is indeed highly advantageous in facilitating electron-hole separation [52]. Furthermore, a charge transfer conduit exists between ZnO and PNS-C, facilitating the electron transfer from the excited state of ZnO to PNS-C via photoinduction. Consequently, the recombination of photoexcited carriers in ZnO is essentially impeded by the redistribution of charge density. Notably, the highly energetic π-electrons confined within the ZnO/PNS-C composite can efficiently migrate to the PNS-C, leading to enhanced electron-hole pair migration and an increased photoexcitation rate. Fig. 4c exhibits photographs of the PNS-C and PNS-C/ZnO composite under visible light and UV irradiation, which clearly show their fluorescence properties. To further investigate the optical properties of our samples, their bandgap energies were computed using the Tauc plot technique [53]. As plotted in Fig. 5, the bandgap energy values of the pristine PNS-C and ZnO are 2.5 and 3.3 eV, respectively. Fig. 5c exhibits two intercept lines with values of 2.5 and 3.1 eV, which relate to the bandgap energies of the PNS-C and ZnO, respectively. This result also provides further evidence of the composite formation's success.

3.3. Photo-antibacterial studies

The successful synthesis of PNS-C and ZnO/PNS-C composite has motivated us to further study their applications for photo-antibacterial activity against *E. coli* and *S. aureus* as examples of gram-negative and gram-positive bacteria, respectively. We initially assessed the antibacterial properties of samples by a minimum inhibitory concentrations (MIC) study. As shown in Fig. 6a, the PNS-C has negligible antibacterial activities against *E. coli* and *S. aureus*, whereas pure ZnO inhibits bacterial growth with MIC values of 180 μg/mL and 170 μg/mL, respectively. More importantly, the ZnO/PNS-C composites exhibited excellent antibacterial activities with much lower concentrations of 75 μg/mL and 60 μg/mL, respectively.

We then investigated the relationship between photoexcitation and the rate of bacterial inactivation. LB plates were utilized to present the statistical data from Fig. 6b regarding the antibacterial density against *E. coli* and *S. aureus* after a 10-min treatment with irradiation and non-irradiation, respectively. Even after light exposure, the PNS-C failed to demonstrate any antibacterial activity against *E. coli* and *S. aureus*. In contrast, the ZnO/PNS-C composite demonstrated remarkable antibacterial efficacy when irradiated for 10 min, as evidenced by a more pronounced decline in the density curve and the formation of almost no conies on the LB agar plates against both *E. coli* and *S. aureus*, compared to pure ZnO (Fig. 6c and d). Furthermore, the survival rates of *E. coli* and *S. aureus* were

Table 2
Atomic percentages of each Zn, O, and C in PNS-C, ZnO, and ZnO/PNS-C composite.

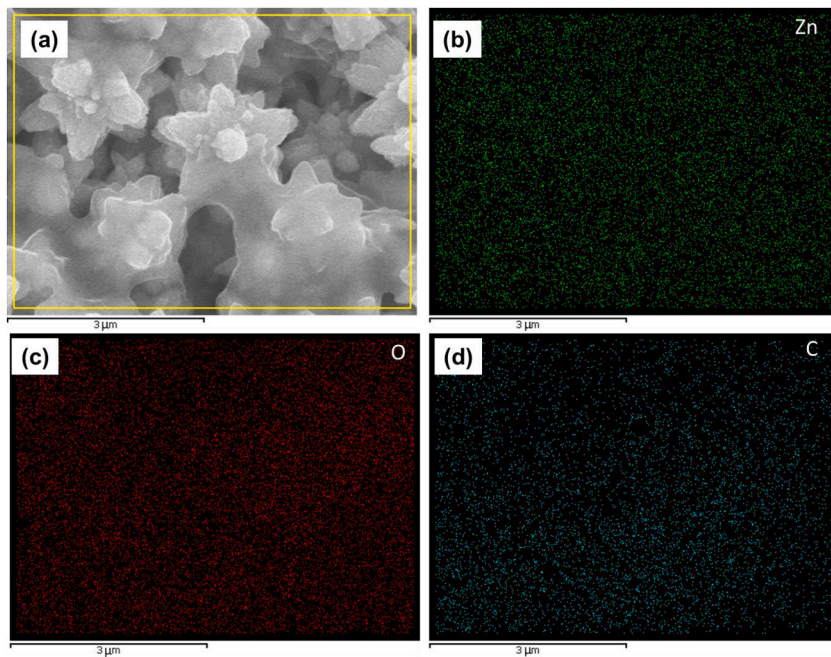| Samples	Zn (%)	O (%)	C (%)
PNS-C	–	29.76	70.24
ZnO	38.63	61.37	–
ZnO/PNS-C	14.60	43.57	41.82

Fig. 3. Elemental mapping of ZnO/PNS-C composite **(a)** SEM image of acquiring signal and elemental mapping of **(b)** zinc, **(c)** oxygen, and **(d)** carbon.
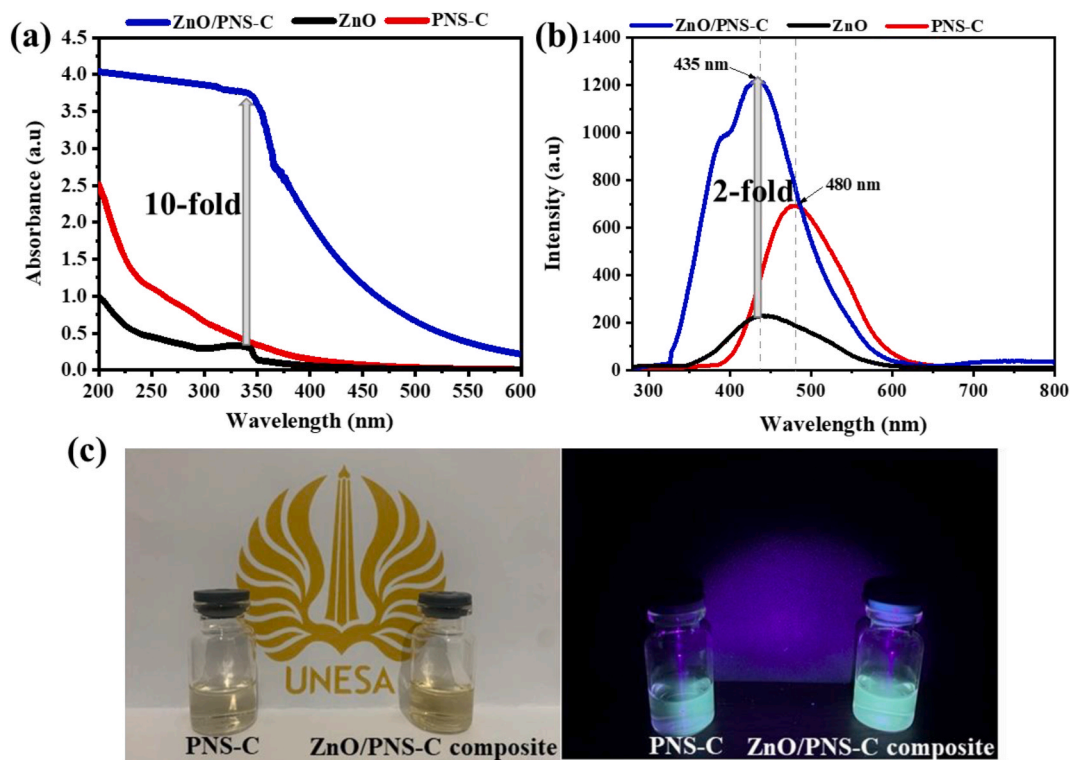

Fig. 4. Optical properties of ZnO, PNS-C and ZnO/PNS-C composites **(a)** UV–Vis spectra and **(b)** PL spectra, and (c) photograph of the samples under visible light and UV irradiation.
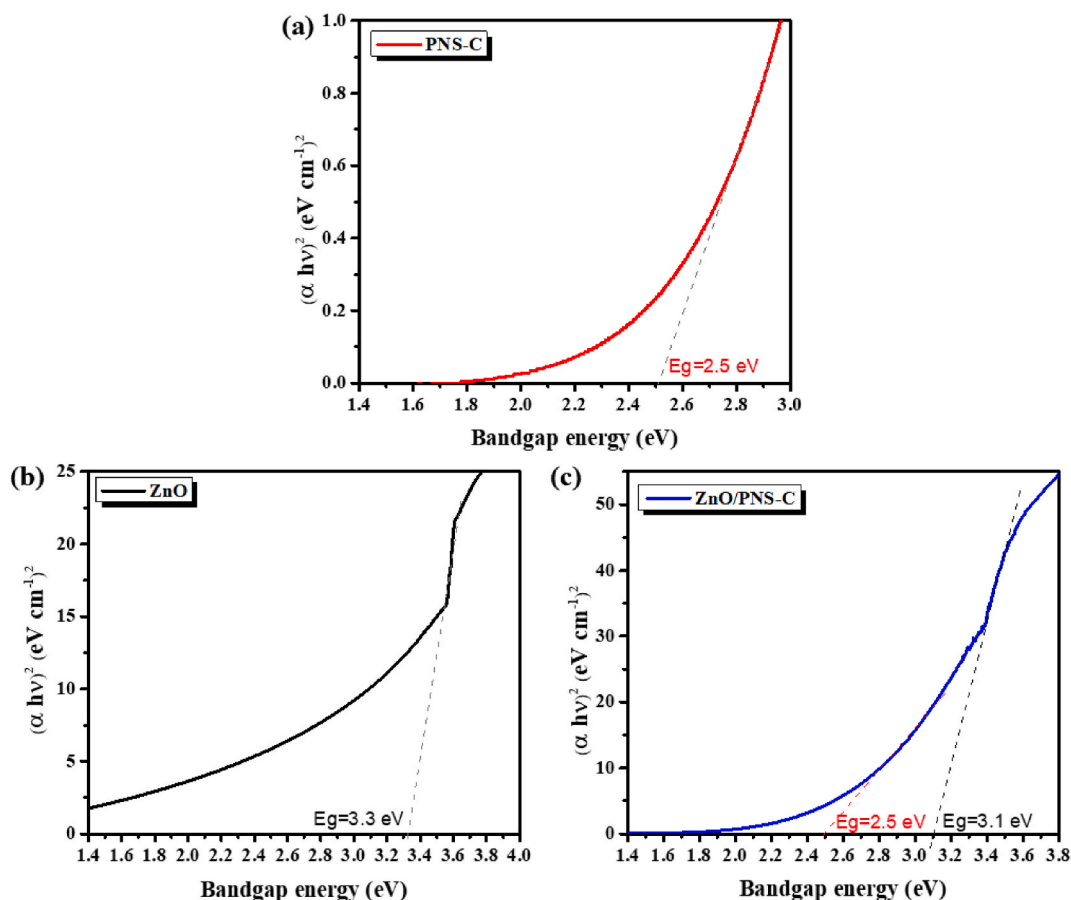
Fig. 5. Bandgap determination of (a) pristine PNS-C, (b) ZnO, and (c) ZnO/PNS-C composite.

determined subsequent to a 10-min irradiation. As illustrated in Fig. 6b, the cell viability of the ZnO/PNS-C composite only remained 90×10^4 CFU/mL, representing a 4.46-fold reduction in the bacterial survival rate relative to pure ZnO. This finding indicates that formation of the ZnO/PNS-C composite produce of a greater quantity of ROS in deactivated bacteria.

3.4. Cytotoxicity evaluation

A MTT assay was performed on RAW cells 264.7 to evaluate the cytotoxicity of the ZnO-PNS-C composite. As depicted in Fig. 7, RAW 264.7 cells remained viable and intact after a 24-h incubation using ZnO/PNS-C, with no cell loss observed. Indeed, even when the concentration was elevated to 250 μg/mL−1, the cell survival rate slightly increased. These findings indicate that ZnO/PNS-C composites are non-toxic to humans and hold promise for application in the treatment of bacterial infections, rendering them a potential and promising antibacterial agent.

3.5. Antibacterial mechanism

Despite extensive research on composites as antibacterial materials, the exact antibacterial mechanism remains unclear, especially for specific bacterial types. The mechanism by which reactive oxygen species (ROS) like $OH^{\bullet}$, $O_2^{\bullet-}$, and H_2O_2 induce bacterial cell death has been explained in several studies [54–56]. Fig. 8a shows the EPR spectra of ZnO-PNS-C in DMPO solution. It is clearly evident that the EPR signal after 5 min of irradiation is much stronger than in the dark condition. This indicates that a greater amount of ROS is produced when the samples are exposed to light. Among the various ROS, including $OH^{\bullet}$, $O_2^{\bullet-}$, and H_2O_2, hydrogen peroxide stands out as the most unstable one capable of permeating biological membranes (lipid peroxidation), leading to mutagenesis. When incoming photon have more energy than the semiconductor catalyst' bandgap energy, surface oxidation and reduction processes help in generating ROS with the aid of photo-generated electrons and holes. Nevertheless, the effectiveness of a photocatalyst hinges on several factors, such as the processes of photoexcitation, bulk diffusion, and surface diffusion. Therefore, the chemical properties, semiconducting behaviour, crystalline structure, and surface morphology of the photocatalyst significantly influence its efficiency. Also, these photocatalysts should have electron transport properties that are kinetically favorable. This will make it easier for electrons to move from the photocatalyst surfaces to the water interface, reducing energy loss through charge transport and photogenerated
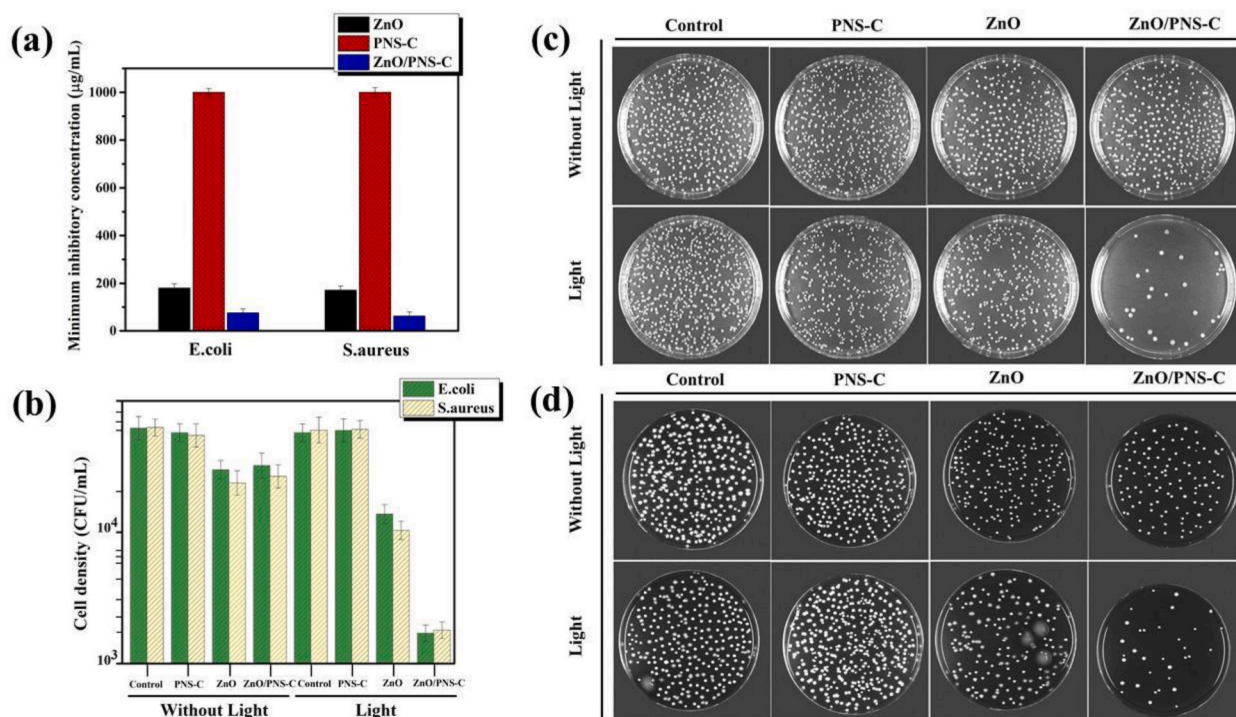
Fig. 6. (a) Antibacterial data as MIC value of ZnO, PNS-C and ZnO/PNS-C composites **(b)** Quantitative results of bacterial inactivation of ZnO, PNS-C and ZnO/PNS-C composites after irradiated with intensity of 50 mW/cm^2 for 10 min. The growth of colonies with irradiated and non-irradiated samples **(c)** *E. coli* **(d)** *S. aureus*.
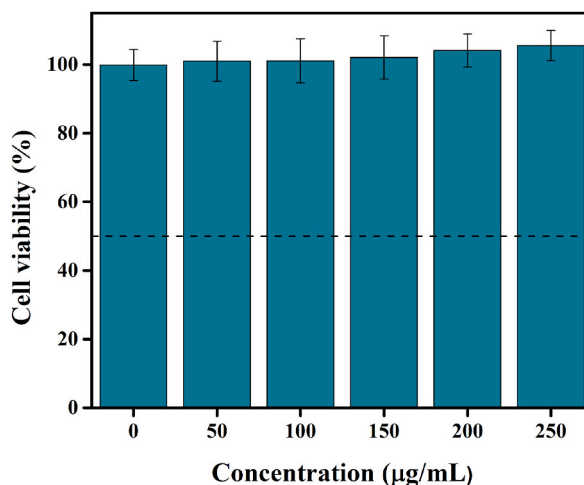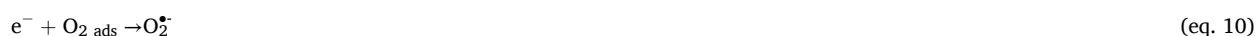

Fig. 7. Cytotoxicity of the ZnO/PNS-C composite evaluated towards RAW cells 264.7.

carrier recombination [57]. To facilitate the effective transportation of active radical species across the bacterial membrane wall, it is crucial for the catalyst to establish strong contact with the bacteria. To make electrostatic interactions with the negatively charged bacterial wall [58], it is very important to keep the catalyst's surface charge positive. In the process of bactericidal action, certain reactions that lead to the formation of ROS are described as follows: Fig. 8b schematically illustrates the bactericidal mechanism of the ZnO/PNS-C composite, involving the free radical species/ROS generation induced by photogenerated holes and electrons. It is important to note that ZnO/PNS-C composites can directly engage with the bacterial cell membrane through electrostatic interactions. This is possible because the p-type material has a positive charge and the bacterial cell wall has a negative charge [59,60]. Thus, even at low concentrations, H_2O_2 can effectively eliminate bacteria by causing damage to their DNA and enzymes [61]. Once lipid per-oxidation has been initiated by H_2O_2, other ROS, such as hydroxyl (OH$^{\bullet}$) and superoxide anion (O$_2^{\bullet -}$), can readily penetrate the
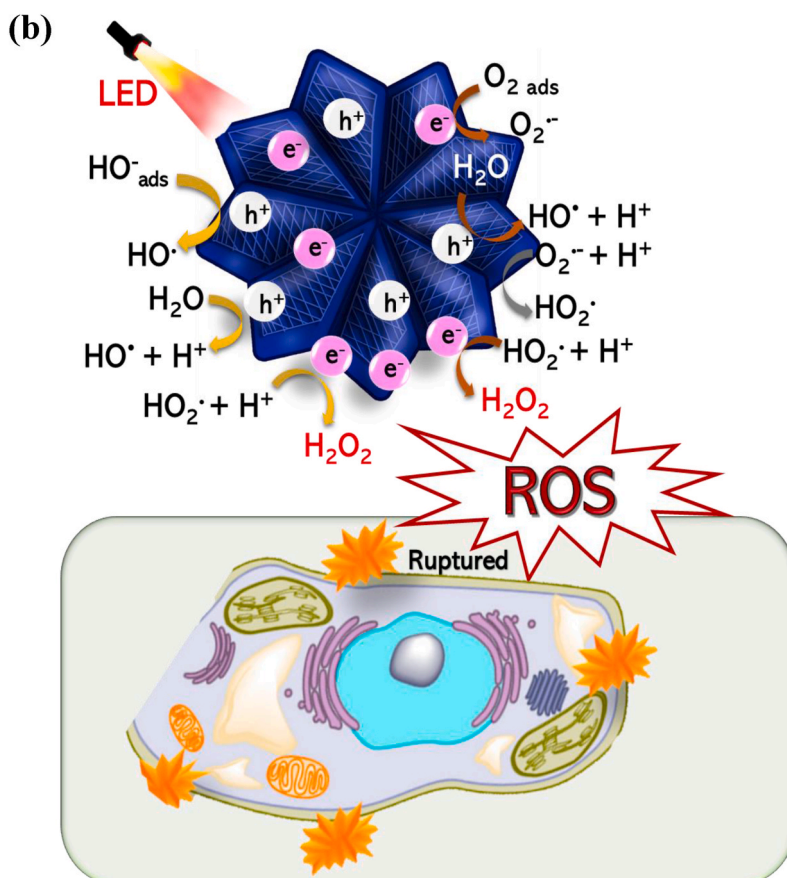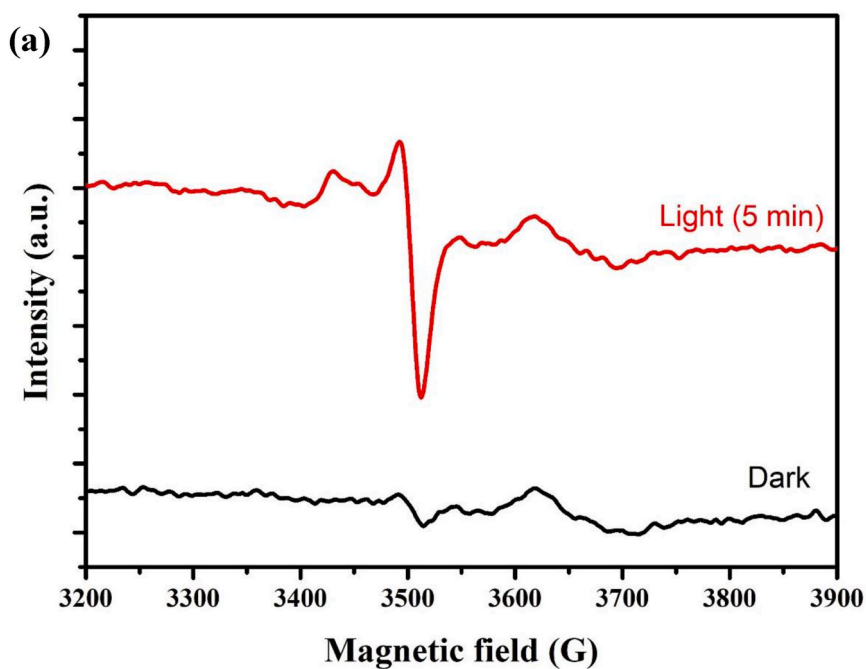
Fig. 8. (a) EPR spectra in DMPO solution before and after light irradiation and (b) antibacterial mechanism of ZnO/PNS-C composites against *E. coli* and *S. aureus* with photo-generated electron-hole induces ROS to rupture cell wall.

bacterial cell wall, causing harm to the organelles within the bacterial cell by acting as both reductants and oxidants [62]. Due to the relatively short lifespan of hydroxyl species, their oxidation capacity is constrained when it comes to penetrating the bacterial cell wall, and they do not directly inflict damage on the bacterial cell. Moreover, as a result of the photocatalytic reactions, the generation of photo-generated electrons (e$^-$) and holes (h$^+$) occurs, leading to the production of H_2O_2, a potent species [60], which plays a role in swiftly deactivating bacterial activities, as demonstrated in Equations (6-13) [63]. Although, HO$^\bullet$ formed, as shown in Equation (8) possesses oxidative capabilities, its brief lifespan restricts its ability to permeate the bacterial cell membrane [64]. The reaction between $O_2^{\bullet-}$ and H_2O_2 radical species inside the bacterial cell results the formation of HO$^\bullet$ as depicted in Equation (13) after penetrating the cell membrane. This underscores the significant role of that HO$^\bullet$ species in deactivating the bacterial [65]. Our finding shows that the bactericidal effects were notably more pronounced when exposed to light illumination compared to conditions in the absence of light. Overall, the ZnO/PNS-C has a lot potential to make photo-antibacterial therapy more effective and efficient.

$$\text{ZnO/PNS-C} + h\nu \rightarrow \text{ZnO/PNS-C (e}^- + \text{h}^+) \tag{eq. 7}$$

$$\text{h}^+ + H_2O \rightarrow HO^\bullet + H^+ \tag{eq. 8}$$

$$\text{h}^+ + HO_{ads}^- \rightarrow HO^\bullet \tag{eq. 9}$$

$$\text{e}^- + O_{2\,ads} \rightarrow O_2^{\bullet-} \tag{eq. 10}$$

$$O_2^{\bullet-} + H^+ \rightarrow HO_2^\bullet \tag{eq. 11}$$

$$\text{e}^- + H_2O + H^+ \rightarrow H_2O_2 \tag{eq. 12}$$

$$H_2O_2 + O_2^{\bullet-} \rightarrow OH^\bullet + OH^- + O_2 \tag{eq. 13}$$

4. Conclusions

In summary, we present the hydrothermal synthesis of a novel star-shaped ZnO/PNS-C composite derived from natural peanut shell biowaste. This composite demonstrates extremely potent antibacterial properties and may be able to surmount certain limitations of existing carbon-based materials. With its high photostability and ability to generate electron holes, the resulting composite exhibited distinctive optical properties. ZnO/PNS-C exhibited remarkable photo-antibacterial activity, inhibiting bacterial growth significantly more than pure ZnO. This is attributed to the enhanced light absorption capability electron-hole separation facilitated by ZnO/PNS-C, which generates a greater quantity of reactive oxygen species (ROS). Therefore, this star-shaped composite material made from a natural bio-waste may contribute to the development of photo-antibacterial therapy with affordable price, abundance, and non-toxicity in future applications.

Data availability

Data will be made available on request.

CRediT authorship contribution statement

Fasih Bintang Ilhami: Writing – original draft, Visualization, Supervision, Resources, Methodology, Investigation, Funding acquisition, Conceptualization. **Fitriana:** Methodology, Data curation, Methodology, Data curation. **Tjandrawati Mozef:** Methodology, Data curation. **Muh Nur Khoiru Wihadi:** Methodology, Data curation. **Munasir:** Writing – review & editing, Supervision, Investigation, Writing – review & editing, Supervision, Investigation. **Mufidatul Khasanah:** Writing – review & editing, Methodology, Investigation. **Nugrahani Primary Putri:** Writing – review & editing, Methodology, Investigation. **Diah Hari Kusumawati:** Writing – review & editing, Methodology, Investigation. **Chen-Yu Kao:** Writing – review & editing, Supervision, Investigation. **Dong-Hau Kuo:** Resources, Conceptualization. **Noto Susanto Gultom:** Writing – review & editing, Investigation, Conceptualization.

Declaration of competing interest

The authors declare that they have no known competing financial interests or personal relationships that could have appeared to influence the work reported in this paper.

Dosen Pemula 2023.

References

[1] K.E. Jones, N.G. Patel, M.A. Levy, A. Storeygard, D. Balk, J.L. Gittleman, P. Daszak, Global trends in emerging infectious diseases, Nature 451 (7181) (2008) 990–993, https://doi.org/10.1038/nature06536.

[2] C. Liu, D. Kong, P.-C. Hsu, H. Yuan, H.-W. Lee, Y. Liu, H. Wang, S. Wang, K. Yan, D. Lin, P.A. Maraccini, K.M. Parker, A.B. Boehm, Y. Cui, Rapid water disinfection using vertically aligned MoS2 nanofilms and visible light, Nat. Nanotechnol. 11 (12) (2016) 1098–1104, https://doi.org/10.1038/nnano.2016.138.

[3] J. Shi, M. Wang, Z. Sun, Y. Liu, J. Guo, H. Mao, F. Yan, Aggregation-induced emission-based ionic liquids for bacterial killing, imaging, cell labeling, and bacterial detection in blood cells, Acta Biomater. 97 (2019) 247–259, https://doi.org/10.1016/j.actbio.2019.07.039.

[4] J. Guo, Y. Qian, B. Sun, Z. Sun, Z. Chen, H. Mao, B. Wang, F. Yan, Antibacterial amino acid-based poly(ionic liquid) membranes: effects of chirality, chemical bonding type, and application for MRSA skin infections, ACS Appl. Bio Mater. 2 (10) (2019) 4418–4426, https://doi.org/10.1021/acsabm.9b00619.

[5] L. Wang, X. Zhang, X. Yu, F. Gao, Z. Shen, X. Zhang, S. Ge, J. Liu, Z. Gu, C. Chen, An all-organic semiconductor C3N4/PDINH heterostructure with advanced antibacterial photocatalytic therapy activity, Adv. Mater. 31 (33) (2019) 1901965, https://doi.org/10.1002/adma.201901965.

[6] S.B. Levy, B. Marshall, Antibacterial resistance worldwide: causes, challenges and responses, Nat. Med. 10 (12) (2004) S122–S129, https://doi.org/10.1038/nm1145.

[7] M.A. Cooper, D. Shlaes, Fix the antibiotics pipeline, Nature 472 (7341) (2011), https://doi.org/10.1038/472032a, 32-32.

[8] Z.-m. Xiu, Q.-b. Zhang, H.L. Puppala, V.L. Colvin, P.J.J. Alvarez, Negligible particle-specific antibacterial activity of silver nanoparticles, Nano Lett. 12 (8) (2012) 4271–4275, https://doi.org/10.1021/nl301934w.

[9] H. Ren, P. Koshy, W.-F. Chen, S. Qi, C.C. Sorrell, Photocatalytic materials and technologies for air purification, J. Hazard Mater. 325 (2017) 340–366, https://doi.org/10.1016/j.jhazmat.2016.08.072.

[10] C. Zhang, J. Guo, X. Zou, S. Guo, Y. Guo, R. Shi, F. Yan, Acridine-based covalent organic framework photosensitizer with broad-spectrum light absorption for antibacterial photocatalytic therapy, Adv. Healthcare Mater. 10 (19) (2021) 2100775, https://doi.org/10.1002/adhm.202100775.

[11] X. Hu, H. Zhang, Y. Wang, B.-C. Shiu, J.-H. Lin, S. Zhang, C.-W. Lou, T.-T. Li, Synergistic antibacterial strategy based on photodynamic therapy: progress and perspectives, Chem. Eng. J. 450 (2022) 138129, 0.1016/j.cej.2022.138129.

[12] M. Lan, S. Zhao, X. Wei, K. Zhang, Z. Zhang, S. Wu, P. Wang, W. Zhang, Pyrene-derivatized highly fluorescent carbon dots for the sensitive and selective determination of ferric ions and dopamine, Dyes Pigments 170 (2019) 107574, https://doi.org/10.1016/j.dyepig.2019.107574.

[13] W. Wang, G. Li, D. Xia, T. An, H. Zhao, P.K. Wong, Photocatalytic nanomaterials for solar-driven bacterial inactivation: recent progress and challenges, Environ. Sci.: Nano 4 (4) (2017) 782–799, https://doi.org/10.1039/C7EN00063D.

[14] Y. Wu, L. Zhang, Y. Zhou, L. Zhang, Y. Li, Q. Liu, J. Hu, J. Yang, Light-induced ZnO/Ag/rGO bactericidal photocatalyst with synergistic effect of sustained release of silver ions and enhanced reactive oxygen species, Chin. J. Catal. 40 (5) (2019) 691–702, https://doi.org/10.1016/S1872-2067(18)63193-6.

[15] X. Pan, W. Dong, J. Zhang, Z. Xie, W. Li, H. Zhang, X. Zhang, P. Chen, W. Zhou, B. Lei, TiO2/Chlorophyll S-Scheme composite photocatalyst with improved photocatalytic bactericidal performance, ACS Appl. Mater. Interfaces 13 (33) (2021) 39446–39457, https://doi.org/10.1021/acsami.1c10892.

[16] A. Schlachter, P.D. Harvey, Properties and applications of copper halide-chalcogenoether and -chalcogenone networks and functional materials, J. Mater. Chem. C 9 (21) (2021) 6648–6685, https://doi.org/10.1039/D1TC00585E.

[17] J. Guo, J. Zhou, Z. Sun, M. Wang, X. Zou, H. Mao, F. Yan, Enhanced photocatalytic and antibacterial activity of acridinium-grafted g-C3N4 with broad-spectrum light absorption for antimicrobial photocatalytic therapy, Acta Biomater. 146 (2022) 370–384, https://doi.org/10.1016/j.actbio.2022.03.052.

[18] P. Chanhom, N. Charoenlap, C. Manipuntee, N. Insin, Metalloporphyrins-sensitized titania-silica-iron oxide nanocomposites with high photocatalytic and bactericidal activities under visible light irradiation, J. Magn. Magn Mater. 475 (2019) 602–610, https://doi.org/10.1016/j.jmmm.2018.11.090.

[19] S. Xu, W. Lu, S. Chen, Z. Xu, T. Xu, V.K. Sharma, W. Chen, Colored TiO2 composites embedded on fabrics as photocatalysts: decontamination of formaldehyde and deactivation of bacteria in water and air, Chem. Eng. J. 375 (2019) 121949, https://doi.org/10.1016/j.cej.2019.121949.

[20] J. Podporska-Carroll, A. Myles, B. Quilty, D.E. McCormack, R. Fagan, S.J. Hinder, D.D. Dionysiou, S. Pillai, Antibacterial properties of F-doped ZnO visible light photocatalyst, J. Hazard Mater. 324 (2017) 39–47, https://doi.org/10.1016/j.jhazmat.2015.12.038.

[21] B. Leng, X. Zhang, S. Chen, J. Li, Z. Sun, Z. Ma, W. Yang, B. Zhang, K. Yang, S. Guo, Highly efficient visible-light photocatalytic degradation and antibacterial activity by GaN:ZnO solid solution nanoparticles, J. Mater. Sci. Technol. 94 (2021) 67–76, https://doi.org/10.1016/j.jmst.2021.04.014.

[22] Q. Xin, H. Shah, A. Nawaz, W. Xie, M.Z. Akram, A. Batool, L. Tian, S.U. Jan, R. Boddula, B. Guo, Q. Liu, J.R. Gong, Antibacterial carbon-based nanomaterials, Adv. Mater. 31 (45) (2019) 1804838, https://doi.org/10.1002/adma.201804838.

[23] K. Shen, X. Chen, J. Chen, Y. Li, Development of MOF-derived carbon-based nanomaterials for efficient catalysis, ACS Catal. 6 (9) (2016) 5887–5903, https://doi.org/10.1021/acscatal.6b01222.

[24] Q. Wang, M. Zhou, Y. Zhang, M. Liu, W. Xiong, S. Liu, Large surface area porous carbon materials synthesized by direct carbonization of banana peel and citrate salts for use as high-performance supercapacitors, J. Mater. Sci. Mater. Electron. 29 (5) (2018) 4294–4300, https://doi.org/10.1007/s10854-017-8376-2.

[25] T. Do Minh, J. Song, A. Deb, L. Cha, V. Srivastava, M. Sillanpää, Biochar based catalysts for the abatement of emerging pollutants: a review, Chem. Eng. J. 394 (2020) 124856, https://doi.org/10.1016/j.cej.2020.124856.

[26] A. Bianco, H.-M. Cheng, T. Enoki, Y. Gogotsi, R.H. Hurt, N. Koratkar, T. Kyotani, M. Monthioux, C.R. Park, J.M.D. Tascon, J. Zhang, All in the graphene family – a recommended nomenclature for two-dimensional carbon materials, Carbon 65 (2013) 1–6, https://doi.org/10.1016/j.carbon.2013.08.038.

[27] S.N. Baker, G.A. Baker, Luminescent carbon nanodots: emergent nanolights, Angew. Chem. Int. Ed. 49 (38) (2010) 6726–6744, https://doi.org/10.1002/anie.200906623.

[28] X. Dong, A.E. Bond, N. Pan, M. Coleman, Y. Tang, Y.-P. Sun, L. Yang, Synergistic photoactivated antimicrobial effects of carbon dots combined with dye photosensitizers, Int. J. Nanomed. 13 (2018) 8025–8035, https://doi.org/10.2147/IJN.S183086.

[29] M.J. Meziani, X. Dong, L. Zhu, L.P. Jones, G.E. LeCroy, F. Yang, S. Wang, P. Wang, Y. Zhao, L. Yang, R.A. Tripp, Y.-P. Sun, Visible-light-activated bactericidal functions of carbon "quantum" dots, ACS Appl. Mater. Interfaces 8 (17) (2016) 10761–10766, https://doi.org/10.1021/acsami.6b01765.

[30] A. Kołodziejczak-Radzimska, T. Jesionowski, Zinc oxide—from synthesis to application, A Review, Materials (2014) 2833–2881, https://doi.org/10.3390/ma7042833.

[31] A.B. Djurišić, X. Chen, Y.H. Leung, A. Man, Ching Ng, ZnO nanostructures: growth, properties and applications, J. Mater. Chem. 22 (14) (2012) 6526–6535, https://doi.org/10.1039/C2JM15548F.

[32] A. Sirelkhatim, S. Mahmud, A. Seeni, N.H.M. Kaus, L.C. Ann, S.K.M. Bakhori, H. Hasan, D. Mohamad, Review on zinc oxide nanoparticles: antibacterial activity and toxicity mechanism, Nano-Micro Lett. 7 (3) (2015) 219–242, https://doi.org/10.1007/s40820-015-0040-x.

[33] R.Y. Hong, J.H. Li, L.L. Chen, D.Q. Liu, H.Z. Li, Y. Zheng, J. Ding, Synthesis, surface modification and photocatalytic property of ZnO nanoparticles, Powder Technol. 189 (3) (2009) 426–432, https://doi.org/10.1016/j.powtec.2008.07.004.

[34] S. Chakrabarti, B.K. Dutta, Photocatalytic degradation of model textile dyes in wastewater using ZnO as semiconductor catalyst, J. Hazard Mater. 112 (3) (2004) 269–278, https://doi.org/10.1016/j.jhazmat.2004.05.013.

[35] F. Xu, P. Zhang, A. Navrotsky, Z.-Y. Yuan, T.-Z. Ren, M. Halasa, B.-L. Su, Hierarchically assembled porous ZnO nanoparticles: synthesis, surface energy, and photocatalytic activity, Chem. Mater. 19 (23) (2007) 5680–5686, https://doi.org/10.1021/cm071190g.

[36] S. Kim, B.E. Dale, Global potential bioethanol production from wasted crops and crop residues, Biomass Bioenergy 26 (4) (2004) 361–375, https://doi.org/10.1016/j.biombioe.2003.08.002.

[37] D. Bhaduri, A. Saha, D. Desai, H.N. Meena, Restoration of carbon and microbial activity in salt-induced soil by application of peanut shell biochar during short-term incubation study, Chemosphere 148 (2016) 86–98, https://doi.org/10.1016/j.chemosphere.2015.12.130.

[38] X. Ma, Y. Dong, H. Sun, N. Chen, Highly fluorescent carbon dots from peanut shells as potential probes for copper ion: the optimization and analysis of the synthetic process, Mater. Today Chem. 5 (2017) 1–10, https://doi.org/10.1016/j.mtchem.2017.04.004.

[39] M. Xue, Z. Zhan, M. Zou, L. Zhang, S. Zhao, Green synthesis of stable and biocompatible fluorescent carbon dots from peanut shells for multicolor living cell imaging, New J. Chem. 40 (2) (2016) 1698–1703, https://doi.org/10.1039/C5NJ02181B.

[40] H. Bozetine, Q. Wang, A. Barras, M. Li, T. Hadjersi, S. Szunerits, R. Boukherroub, Green chemistry approach for the synthesis of ZnO–carbon dots nanocomposites with good photocatalytic properties under visible light, J. Colloid Interface Sci. 465 (2016) 286–294, https://doi.org/10.1016/j.jcis.2015.12.001.

[41] N.S. Gultom, H. Abdullah, D.-H. Kuo, Phase transformation of bimetal zinc nickel oxide to oxysulfide photocatalyst with its exceptional performance to evolve hydrogen, Appl. Catal. B Environ. 272 (2020) 118985, https://doi.org/10.1016/j.apcatb.2020.118985.

[42] N.S. Gultom, H. Abdullah, D.-H. Kuo, Effects of graphene oxide and sacrificial reagent for highly efficient hydrogen production with the costless Zn(O,S) photocatalyst, Int. J. Hydrogen Energy 44 (56) (2019) 29516–29528, https://doi.org/10.1016/j.ijhydene.2019.08.066.

[43] R.F. Zhuo, H.T. Feng, Q. Liang, J.Z. Liu, J.T. Chen, D. Yan, J.J. Feng, H.J. Li, S. Cheng, B.S. Geng, X.Y. Xu, J. Wang, Z.G. Wu, P.X. Yan, G.H. Yue, Morphology-controlled synthesis, growth mechanism, optical and microwave absorption properties of ZnO nanocombs, J. Phys. Appl. Phys. 41 (18) (2008) 185405, https://doi.org/10.1088/0022-3727/41/18/185405.

[44] M. Silambarasan, S. Shanmugam, T. Soga, Raman and photoluminescence studies of Ag and Fe-doped ZnO nanoparticles, Int. J. ChemTech Res. 7 (2015) 1644–1650.

[45] X. Zhang, J. Pan, C. Zhu, Y. Sheng, Z. Yan, Y. Wang, B. Feng, The visible light catalytic properties of carbon quantum dots/ZnO nanoflowers composites, J. Mater. Sci. Mater. Electron. 26 (5) (2015) 2861–2866, https://doi.org/10.1007/s10854-015-2769-x.

[46] L. Zhang, H. Cheng, R. Zong, Y. Zhu, Photocorrosion suppression of ZnO nanoparticles via hybridization with graphite-like carbon and enhanced photocatalytic activity, J. Phys. Chem. C 113 (6) (2009) 2368–2374, https://doi.org/10.1021/jp807778r.

[47] B. De, N. Karak, A green and facile approach for the synthesis of water soluble fluorescent carbon dots from banana juice, RSC Adv. 3 (22) (2013) 8286–8290, https://doi.org/10.1039/C3RA00088E.

[48] Y. Li, B.-P. Zhang, J.-X. Zhao, Z.-H. Ge, X.-K. Zhao, L. Zou, ZnO/carbon quantum dots heterostructure with enhanced photocatalytic properties, Appl. Surf. Sci. 279 (2013) 367–373, https://doi.org/10.1016/j.apsusc.2013.04.114.

[49] N. Siregar Motlan, J.H. Panggabean, M. Sirait, J. Rajagukguk, N.S. Gultom, F.K. Sabir, Fabrication of dye-sensitized solar cells (DSSC) using Mg-doped ZnO as photoanode and extract of rose myrtle (Rhodomyrtus tomentosa) as natural dye, Int. J. Photoenergy 2021 (2021) 4033692, https://doi.org/10.1155/2021/4033692.

[50] P.B. Pati, G. Damas, L. Tian, D.L.A. Fernandes, L. Zhang, I.B. Pehlivan, T. Edvinsson, C.M. Araujo, H. Tian, An experimental and theoretical study of an efficient polymer nano-photocatalyst for hydrogen evolution, Energy Environ. Sci. 10 (6) (2017) 1372–1376, https://doi.org/10.1039/C7EE00751E.

[51] H. vol 3. Zimmermann, Basics of optical emission and absorption, in: Integrated Silicon Optoelectronics. Springer Series in Photonics, Springer, Berlin, Heidelberg, 2000, https://doi.org/10.1007/978-3-662-04018-8_1.

[52] H. Abdullah, N.S. Gultom, D.-H. Kuo, A.D. Saragih, Cobalt-doped Zn(O,S)/Ga2O3 nanoheterojunction composites for enhanced hydrogen production, New J. Chem. 42 (12) (2018) 9626–9634, https://doi.org/10.1039/C7NJ05124G, 9.

[53] H. Shuwanto, H. Abdullah, D.-H. Kuo, N.S. Gultom, Surface active sites of Y-doped Zn(O,S) for chemisorption and hydrogenation of azobenzene and nitroaromatic compounds under light via self-generated proton, Appl. Surf. Sci. 552 (2021) 149508, https://doi.org/10.1016/j.apsusc.2021.149508.

[54] M.M. Abudabbus, I. Jevremović, A. Janković, A. Perić-Grujić, I. Matić, M. Vukašinović-Sekulić, D. Hui, K.Y. Rhee, V. Mišković-Stanković, Biological activity of electrochemically synthesized silver doped polyvinyl alcohol/graphene composite hydrogel discs for biomedical applications, Compos. B Eng. 104 (2016) 26–34, https://doi.org/10.1016/j.compositesb.2016.08.024.

[55] Z. Liu, J. Yan, Y.-E. Miao, Y. Huang, T. Liu, Catalytic and antibacterial activities of green-synthesized silver nanoparticles on electrospun polystyrene nanofiber membranes using tea polyphenols, Compos. B Eng. 79 (2015) 217–223, https://doi.org/10.1016/j.compositesb.2015.04.037.

[56] J.M. Wu, W.T. Kao, Heterojunction nanowires of AgxZn1–xO–ZnO photocatalytic and antibacterial activities under visible-light and dark conditions, J. Phys. Chem. C 119 (3) (2015) 1433–1441, https://doi.org/10.1021/jp510259j.

[57] R.M. Navarro Yerga, M.C. Álvarez Galván, F. del Valle, J.A. Villoria de la Mano, J.L.G. Fierro, Water splitting on semiconductor catalysts under visible-light irradiation, ChemSusChem 2 (6) (2009) 471–485, https://doi.org/10.1002/cssc.200900018.

[58] J.T. Seil, T.J. Webster, Antimicrobial applications of nanotechnology: methods and literature, Int. J. Nanomed. 7 (null) (2012) 2767–2781, https://doi.org/10.2147/IJN.S24805.

[59] I. Matai, A. Sachdev, P. Dubey, S. Uday Kumar, B. Bhushan, P. Gopinath, Antibacterial activity and mechanism of Ag–ZnO nanocomposite on S. aureus and GFP-expressing antibiotic resistant E. coli, Colloids Surf. B Biointerfaces 115 (2014) 359–367, https://doi.org/10.1016/j.colsurfb.2013.12.005.

[60] M. Grkovic, D.B. Stojanovic, V.B. Pavlovic, M. Rajilic-Stojanovic, M. Bjelovic, P.S. Uskokovic, Improvement of mechanical properties and antibacterial activity of crosslinked electrospun chitosan/poly (ethylene oxide) nanofibers, Compos. B Eng. 121 (2017) 58–67, https://doi.org/10.1016/j.compositesb.2017.03.024.

[61] M. Cho, H. Chung, W. Choi, J. Yoon, Different inactivation behaviors of MS-2 phage and Escherichia coli in TiO2 photocatalytic disinfection, Appl. Environ. Microbiol. 71 (1) (2005) 270–275, https://doi.org/10.1128/AEM.71.1.270-275.2005.

[62] H. Rosen, S.J. Klebanoff, Bactericidal activity of a superoxide anion-generating system. A model for the polymorphonuclear leukocyte, J. Exp. Med. 149 (1) (1979) 27–39, https://doi.org/10.1084/jem.149.1.27.

[63] Y.-X. Hou, H. Abdullah, D.-H. Kuo, S.-J. Leu, N.S. Gultom, C.-H. Su, A comparison study of SiO2/nano metal oxide composite sphere for antibacterial application, Compos. B Eng. 133 (2018) 166–176, https://doi.org/10.1016/j.compositesb.2017.09.021.

[64] Y. Kikuchi, K. Sunada, T. Iyoda, K. Hashimoto, A. Fujishima, Photocatalytic bactericidal effect of TiO2 thin films: dynamic view of the active oxygen species responsible for the effect, J. Photochem. Photobiol. Chem. 106 (1) (1997) 51–56, https://doi.org/10.1016/S1010-6030(97)00038-5.

[65] J.P. Kehrer, The Haber–Weiss reaction and mechanisms of toxicity, Toxicology 149 (1) (2000) 43–50, https://doi.org/10.1016/S0300-483X(00)00231-6.